Computational Mechanics (1994) 13, 241–254

Computational Mechanics

Large-strain 3D-analysis of fibre-reinforced composites using rebar elements: hyperelastic formulations for cords

G. Meschke, P. Helnwein
Institute for Strength of Materials, Technical University of Vienna, Karlsplatz 13/E202, A-1040 Vienna, Austria

Abstract. The well-known finite element representation of reinforcing bars by means of overlay ("rebar") elements is recast in the context of finite strain analyses of cord-reinforced composite materials. The variational formulation including the linearized forms is presented on the basis of hyperelasticity. Three material laws including two variants of the Neo-Hooekean model and the quadratic logarithmic model are investigated. An explicit formulation for uniaxial stress states is given for the Neo-Hooekean model. A comparative evaluation with regards to computational efficiency and physical plausibility shows that the logarithmic model is optimally suited for this class of problems and for moderately large strains. The rebar-element concept in conjunction with an incompressible finite element formulation for the representation of a rubber matrix material is applied to comparative finite strain FE-analyses of a cord-reinforced rubber sandwich panel, with different hyperelastic models used for modelling of the ply material.

1 Introduction

Finite element analyses of structures made of cord reinforced composite materials require adequate methods to characterize the highly anisotropic behavior induced by one or several layers of parallel fiber bundles (cords) with different spatial orientation embedded in a matrix material. A typical example for this class of structures are automobile tires. Currently most numerical analyses of cord-reinforced composite materials are based on theories and techniques originally developed for laminated fibrous composites, with several arbitrarily oriented cord layers and the matrix material being represented within one single finite element on the basis of an anisotropic constitutive law, see Noor and Tanner (1985), Tabaddor and Stafford (1985), Reddy (1989) and references therein. An alternative computational approach on the basis of so-called rebar elements which previously has been successfully applied in computational mechanics of reinforced concrete structures in the context of the infinitesimal theory, see, e.g., Mang and Meschke (1991), turned out to be remarkably effective in finite strain analyses of cord-reinforced rubber composite material (Helnwein et al. (1993)). This technique completely circumvents the drawbacks associated with "averaging formulations" without significant additional computational efforts. In particular, it provides a mechanically proper description of the different constituents in the framework of large strain theories. The merits of this approach are discussed in detail in Sect. 2.

Section 3 contains the variational formulation for a single fibre on the basis of hyperelasticity, remarks on the implementation in a finite element code are given in Sect. 4. In Sect. 5 different material models are re-formulated for the special case of uniaxial stress states. Two models belong to the class of Neo-Hookean material laws (Sect. 5.1). Explict expressions for the axial stress-stretch relationship and for the uniaxial tangent modulus, respectively, are given for one variant of these formulations. In Sect. 5.2 the quadratic logarithmic model is proposed as an effective alternative approach suitable for most practical applications.

Section 6 contains a comparative evaluation of these three models, along with the still widley employed St. Venant Model, with regards to their computational effectiveness and their uniaxial stress-stretch characteristics at large strains, respectively.

In Sect. 7, the influence of the different formulations with regards to the predicted structural response is illustrated in the context of FE-analyses of a cord-reinforced rubber sandwich panel.

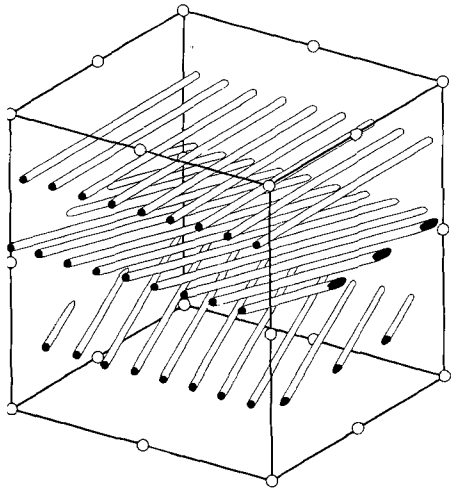

Fig. 1. Modelling of cord-reinforced composites by "Rebar"—elements

2 Remarks on rebar-elements

Rebar elements may be characterized as "overlay" elements that represent one or more cord layers with arbitrary orientation in conjunction with corresponding elements representing the matrix material (Fig. 2). The matrix element and the "overlay" element share the same nodal points. Therefore, no additional degrees of freedom are introduced. A recent paper by Helnwein et al. (1993) demonstrated, that this well known methodology which has been employed successfully in computational mechanics of reinforced concrete structures is well suited for the analysis of reinforced composite materials when extended to the large strain regime. This approach possesses a number of desireable features when compared to standard models based on techniques developed for laminated fibrous materials:

- The different components—several unidirectional laminae and the matrix material—are represented completely separately. In the case of rubber matrix material, for instance, a non-linear elastic law such as the Mooney material law may be applied altogether with a mixed finite element formulation to account for the incompressible character of rubber. As far as the cord layers are concerned, formulations of the Neo-Hookean type with different material parameters for different layers within one element may be applied. Consideration of micro buckling or of plastification of the cords does not constitute any additional difficulties.
- Several cord layers may be represented within one single element without inducing any additional discretization error. This makes the use of rebar elements particularly efficient in large scale 3D analyses.
- Experimentally obtained material parameters for the individual components may be used directly as input parameters for the analyses.
- The (true) stress state is obtained separately in the different plies and in the matrix material, respectively.

3 Kinematics, weak form and its linearization for the 1-D case

In this section we give a summary of the basic kinematics, the weak form and its exact linearization on the basis of hyperelasticity for the special case of a one dimensional fibre with arbitrary spatial orientation.

Coordinates $\mathbf{X}_A \in \mathscr{B}$ in the reference configuration are associated with corresponding coordinates $\mathbf{x}_A$ of a point $\mathbf{A}$ in the deformed (spatial) configuration by the map $\mathbf{x}_A = \boldsymbol{\varphi}(\mathbf{X}_A)$. In what follows, a single fiber ("rebar") with its orientation defined in the *reference configuration* by the unit vector

$\mathbf{T}$ is considered. The corresponding unit vector $\mathbf{t}$ in the *spatial configuration* is given by

$$\lambda_R \mathbf{t} = \mathbf{F}\mathbf{T} \tag{1}$$

where λ_R is the axial stretch of the fibre and $\mathbf{F}$ denotes the deformation gradient of the composite material. Multiplying Eq. (1) by $\mathbf{F}^T$ and by $\mathbf{T}^T$, respectively, the stretch λ_R may be expressed in terms of the Right Cauchy–Green tensor $\mathbf{C} = \mathbf{F}^T\mathbf{F}$ and of $\mathbf{T}$ as

$$\lambda_R^2 = \mathbf{T}^T\mathbf{C}\mathbf{T}. \tag{2}$$

The deformation of the rebar fibre is characterized by a modified Right Cauchy–Green tensor, $\mathbf{C}_R$, defined by its spectral decomposition

$$\mathbf{C}_R = \lambda_R^2 \mathbf{T} \otimes \mathbf{T} + \sum_{A=1,2} \lambda_{L,A}^2 \mathbf{L}^A \otimes \mathbf{L}^A, \tag{3}$$

where $\lambda_{L,A}$ denote the lateral stretches and $\mathbf{L}^A$ are unit vectors orthogonal to $\mathbf{T}$. The underlying assumption of axisymmetry of the deformation of one single fibre implies that $\lambda_{L,1} = \lambda_{L,2}$. Equation (3) then takes the form

$$\mathbf{C}_R = \lambda_R^2 \mathbf{T} \otimes \mathbf{T} + \lambda_L^2 (\mathbf{L}^1 \otimes \mathbf{L}^1 + \mathbf{L}^2 \otimes \mathbf{L}^2). \tag{4}$$

From Eq. (4) it follows, that the direction of the rebar fibre, $\mathbf{T}$, is a principal direction of $\mathbf{C}_R$, and, consequently, the in-plane shear deformations of the plies are neglected. Moreover, the assumption of zero lateral stresses in the fibres implies that $\lambda_L = f(\lambda_R)$. Compatibility with respect to the deformation of the matrix material and the fibre in axial direction requires that

$$\mathbf{T}^T\mathbf{C}_R\mathbf{T} = \lambda_R^2 = \mathbf{T}^T\mathbf{C}\mathbf{T}. \tag{5}$$

The space of admissible variations, $\mathscr{U}$, is defined in the standard form as

$$\mathscr{U} := \{\boldsymbol{\eta} : \boldsymbol{\varphi}(\mathscr{B}) \to \mathbb{R}^3 \mid \boldsymbol{\eta}(\boldsymbol{\varphi}(\mathbf{X})) = \mathbf{O} \quad \text{for} \quad \mathbf{X} \in \partial_{\boldsymbol{\varphi}} \mathscr{B}\} \tag{6}$$

where $\partial_{\boldsymbol{\varphi}} \mathscr{B}$ denotes the part of the boundary $\partial \mathscr{B}$ of the body $\mathscr{B}$ where displacements are prescribed. We further use the notation of $\boldsymbol{\eta}_0 = \boldsymbol{\eta} \circ \boldsymbol{\varphi}$ denoting the admissible material variations.

With this standard notation at hand, the *weak form* expressed in the *spatial configuration* takes the form

$$g(\boldsymbol{\varphi}, \boldsymbol{\eta}) = \int_v \sigma_R \cdot \eta_R' \, dv - g_{ext} \tag{7}$$

where $\eta_R' = \mathbf{t}^T \nabla \boldsymbol{\eta} \mathbf{t}$ is the gradient of the virtual displacements transformed to the rebar direction and g_{ext} denotes the virtual work of the external forces. Noting that

$$\nabla \boldsymbol{\eta} \mathbf{F} = GRAD\, \boldsymbol{\eta}_0 \tag{8}$$

altogether with Eq. (1) yields

$$\eta_R' = \mathbf{t}^T GRAD\, \boldsymbol{\eta}_0 \mathbf{F}^{-1} \mathbf{t} = \frac{1}{\lambda_R} \mathbf{t}^T GRAD\, \boldsymbol{\eta}_0 \mathbf{T}. \tag{9}$$

The relation between the Cauchy stress $\boldsymbol{\sigma}$ and the Second Piola Kirchoff stress $\mathbf{S}$

$$\boldsymbol{\sigma} = \frac{1}{J} \mathbf{F}\mathbf{S}\mathbf{F}^T, \tag{10}$$

with $J = \mathrm{Det}\, \mathbf{F}$, may be specialized to the uniaxial case using Eqs. (1), (2)

$$\sigma_R = \mathbf{t}^T \frac{1}{J} \mathbf{F}\mathbf{S}\mathbf{F}^T \mathbf{t} = \frac{1}{J} \frac{1}{\lambda_R^2} \mathbf{T}^T\mathbf{C}\mathbf{T} S_R \mathbf{T}^T\mathbf{C}\mathbf{T} = \frac{\lambda_R^2}{J} S_R \tag{11}$$

with $\sigma_R = \mathbf{t}^T \boldsymbol{\sigma} \mathbf{t}$ and $S_R = \mathbf{T}^T\mathbf{S}\mathbf{T}$. From Eq. (7) the final result for the weak form expressed in the reference configuration is obtained as

$$G(\boldsymbol{\varphi}, \boldsymbol{\eta}_0) = \int_V S_R \cdot \mathbf{T}^T\mathbf{F}^T GRAD\, \boldsymbol{\eta}_0 \mathbf{T} \, dV - G_{ext}. \tag{12}$$

The constitutive behavior of the rebar fibre is expressed in terms of a stored energy function, W, of the form

$$W(\mathbf{X}, \mathbf{C}_R) = W(\mathbf{X}, \lambda_R, \lambda_L), \tag{13}$$

where Eq. (4) is considered. Note that $W(\mathbf{X}, \lambda_R, \lambda_L)$ is rotationally invariant and, therefore, objectivity of the constitutive response is guaranteed. The Second Piola-Kirchhoff Tensor is obtained from the stored energy function as

$$\mathbf{S} = 2\frac{\partial W}{\partial \mathbf{C}_R} = 2\frac{\partial W}{\partial \lambda_R}\frac{\partial \lambda_R}{\partial \mathbf{C}_R} + 2\frac{\partial W}{\partial \lambda_L}\frac{\partial \lambda_L}{\partial \mathbf{C}_R}. \tag{14}$$

From Eq. (2) the relation

$$2\lambda_R d\lambda_R = \mathbf{T}^T d\mathbf{C}_R \mathbf{T} = d\mathbf{C}_R : \mathbf{T} \otimes \mathbf{T} \tag{15}$$

is obtained, and consequently,

$$\frac{\partial \lambda_R}{\partial \mathbf{C}_R} = \frac{1}{2\lambda_R}\mathbf{T} \otimes \mathbf{T}. \tag{16}$$

Analogously,

$$\frac{\partial \lambda_L}{\partial \mathbf{C}_R} = \frac{1}{2\lambda_L}\mathbf{L}^1 \otimes \mathbf{L}^1 + \mathbf{L}^2 \otimes \mathbf{L}^2. \tag{17}$$

Inserting Eqs. (16) and (17) into Eq. (14), transforming $\mathbf{S}$ into the direction of the rebar fibre and noting that due to orthogonality $\mathbf{L}^A \cdot \mathbf{T} = 0$, $A = 1, 2$, yields

$$S_R(\lambda_R, \lambda_L) = 2\mathbf{T}^T \frac{\partial W(\lambda_R, \lambda_L)}{\partial \lambda_R}\frac{\partial \lambda_R}{\partial \mathbf{C}_R}\mathbf{T} = \frac{\partial W(\lambda_R, \lambda_L)}{\partial \lambda_R}\frac{1}{\lambda_R} = 2\frac{\partial W(\lambda_R, \lambda_L)}{\partial \lambda_R^2}. \tag{18}$$

Substituting $\mathbf{T}$ in Eq. (18) by $\mathbf{T} = \lambda_R \mathbf{F}^{-1}\mathbf{t}$ (Eq. (1)) and noting that

$$\mathbf{T} \otimes \mathbf{T} = \lambda_R^2 \mathbf{F}^{-1}(\mathbf{t} \otimes \mathbf{t})\mathbf{F}^{-T}, \tag{19}$$

the Kirchoff stress tensor, transformed to the direction of the rebar fibre, is obtained as

$$\tau_R(\lambda_R, \lambda_L) = \mathbf{t}^T \boldsymbol{\tau} \mathbf{t} = \mathbf{t}^T \mathbf{F} \mathbf{S} \mathbf{F}^T \mathbf{t} = \frac{\partial W(\lambda_R, \lambda_L)}{\partial \lambda_R}\lambda_R. \tag{20}$$

For the case of uniaxial stress states considered here, the constraint equation

$$\tau_L(\lambda_R, \lambda_L) = \frac{\partial W(\lambda_R, \lambda_L)}{\partial \lambda_L}\lambda_L = 0 \tag{21}$$

determines the relation $\lambda_L = \lambda_L(\lambda_R)$. Hence, linearization of $S_R = S_R(\lambda_R)$ is obtained as

$$dS_R = \frac{dS_R(\lambda_R)}{d\lambda_R^2}\frac{d\lambda_R^2}{d\mathbf{C}} d\mathbf{C}. \tag{22}$$

The first term on the right hand side of in Eq. (22) represents the *uniaxial tangent modulus* which is obtained from the specific hyperelastic model by taking the derivative of Eq. (18),

$$\frac{dS_R}{d\lambda_R^2} = 2\frac{d^2 W(\lambda_R, \lambda_L)}{d(\lambda_R^2)^2}. \tag{23}$$

From Eq. (16) the second term is obtained as

$$\frac{d\lambda_R^2}{d\mathbf{C}} = \mathbf{T} \otimes \mathbf{T}. \tag{24}$$

Linearization of $\mathbf{C}$ is given by the standard result

$$d\mathbf{C} = \mathbf{F}^T GRAD\mathbf{u} + GRAD^T\mathbf{u}\mathbf{F}. \tag{25}$$

With these results at hand, the exact linearization of the weak form Eq. (12) in the reference configuration is readily obtained as

$$\begin{aligned} DG\cdot\boldsymbol{\eta}_0 &= \int_V dS_R\cdot\mathbf{T}^T\mathbf{F}^T GRAD\,\boldsymbol{\eta}_0\mathbf{T}\,dV + \int_V S_R\cdot\mathbf{T}^T\,d\mathbf{F}^T GRAD\,\boldsymbol{\eta}_0\mathbf{T}\,dV \\ &= \int_V \mathbf{T}^T[\mathbf{F}^T GRAD\mathbf{u} + GRAD^T\mathbf{u}\mathbf{F}]\mathbf{T}\cdot\left(\frac{dS_R}{d\lambda_R^2}\right)\cdot\mathbf{T}^T\mathbf{F}^T GRAD\,\boldsymbol{\eta}_0\mathbf{T}\,dV \\ &\quad + \int_V (GRAD\mathbf{u}\,\mathbf{T})^T S_R(GRAD\,\boldsymbol{\eta}_0\mathbf{T})\,dV. \end{aligned} \tag{26}$$

Accordingly, using Eq. (1) and Eq. (8), linearization of the Euler–Lagrange equations expressed in the spatial configuration is obtained as

$$\delta g\cdot\boldsymbol{\eta} = \int_v \mathbf{t}^T\nabla^s\mathbf{u}\,\mathbf{t}\cdot(e_t)\cdot\mathbf{t}^T\nabla\boldsymbol{\eta}^s\mathbf{t}\,dv + \int_v(\nabla\mathbf{u}\,\mathbf{t})^T\cdot\sigma_R\cdot\nabla\boldsymbol{\eta}\,\mathbf{t}\,dv. \tag{27}$$

v is the volume of the body in the current configuration, e_t denotes the uniaxial *spatial tangent modulus*, defined as

$$e_t = \frac{\lambda_R^4}{J}\left(\frac{2dS_R}{d\lambda_R^2}\right) = \frac{\lambda_R^4}{J}E_T, \tag{28}$$

where $E_T = 2dS_R/d\lambda_R^2$ represents the *material tangent modulus* of the rebar fibre, and

$$\nabla^s\mathbf{u} = \tfrac{1}{2}(u_{i,j} + u_{j,i}). \tag{29}$$

4 Remarks on the numerical implementation

The geometry of the rebar layers is defined in the context of 3D isoparametric elements, characterized by the map

$$\mathbf{X}_e^h = \sum_{A=1}^{N}\mathbf{N}_A(\boldsymbol{\xi})\mathbf{X}^A, \tag{30}$$

where $\mathbf{X}_e^h$, $\mathbf{X}^A$ are the interpolated and the nodal coordinates in the reference configuration, respectively, $\mathbf{N}_A(\boldsymbol{\xi})$ are the shape functions, and $\boldsymbol{\xi}^T = [\xi, \eta, \zeta]$ are the natural coordinates in the isoparametric domain and N is the number of nodal points in the element.

Figures 2a and 2b show a typical rebar layer embedded in a 20 node isoparametric element. Figure 2a contains the geometry of the cord layer in the parent element, Fig. 2b illustrates the corresponding configuration in the isoparametric mapping. The numbers 1, 2, 3, 4 denote the integration points in one layer. The spatial position and direction of the rebar fibres is defined for each layer in the isoparametric domain at n integration points (Fig. 2a) by the values $\bar{\zeta}_n$ and $\mathbf{T}_n$,

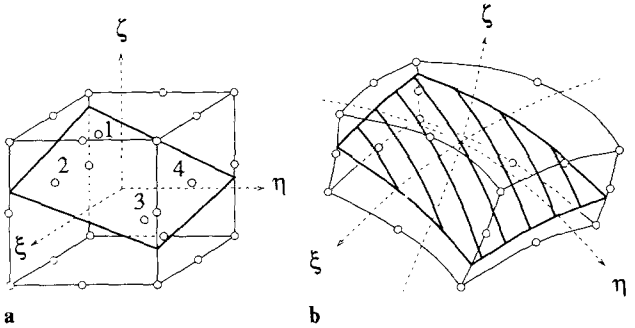

Fig. 2. Typical Rebar layer in a 20-node isoparametric element: **a** geometry in the parent element, **b** geometry in the isoparametric domain

which are input by means of a subroutine. $\bar{\zeta}_n$ denotes the distance of the rebar fibre from the middle surface of the element at each integration point n. The spatial position of a rebar layer within the element is then defined by the shape functions $N_{n,R}$ as

$$\zeta_R(\xi,\eta) = \sum_{A=1}^{n} N_{A,R}(\xi,\eta)\bar{\zeta}_A. \tag{31}$$

In the present context, the geometry of a rebar layer is approximated by a bilinear form defined in the isoparametric parent element, with the natural coordinates of the integration points

$$\bar{\xi} = \pm\frac{1}{\sqrt{3}}, \quad \bar{\eta} = \pm\frac{1}{\sqrt{3}}, \tag{32}$$

and the shape functions $N_{n,R}$ given as

$$\begin{aligned} N_{1,R} &= \tfrac{1}{4}(\sqrt{3}\xi - 1)(\sqrt{3}\eta - 1), \quad N_{2,R} = -\tfrac{1}{4}(\sqrt{3}\xi + 1)(\sqrt{3}\eta - 1) \\ N_{3,R} &= \tfrac{1}{4}(\sqrt{3}\xi + 1)(\sqrt{3}\eta + 1), \quad N_{4,R} = -\tfrac{1}{4}(\sqrt{3}\xi - 1)(\sqrt{3}\eta + 1). \end{aligned} \tag{33}$$

5 One dimensional hyperelastic formulations

In this section, we formulate the constitutive behavior of a general class of (compressible) materials for cord-reinforcements undergoing large deformations for the special case of uniaxial stress states using two different formulations of the standard *Neo-Hookean material model* (Sect. 5.1) and the *quadratic logarithmic model* (Sect. 5.2). A complete summary of the expressions for the function of stored energy, W, the fibre stress S_R, and the uniaxial material tangent modulus E_T for all models including the linear St. Venant Model, is contained in the Appendix.

5.1 Neo-Hooekean Models

A particular formulation of $W(\mathbf{C}_R)$, that has the correct behavior as $J_R \to 0$ and $J_R \to \infty$, see, e.g. Ciarlet (1981) for a detailed discussion, was proposed by Simo and Pister (1985) in the form (*Neo-Hooekean Model I*)

$$W(\mathbf{C}_R) = U(J_R) + \tilde{W}(\mathbf{C}_R) = \tfrac{1}{2}(K - \tfrac{2}{3}G)(\ln J_R)^2 - G\ln J_R + \frac{G}{2}(I_{R,1} - 3) \tag{34}$$

where $I_{R,1} = \operatorname{tr}\mathbf{C}_R$ and K and G correspond to the bulk and the shear modulus of the linear theory, respectively. We remark that this formulation preserves the physical meaning of the Poissons ratio in the large strain regime. In particular, for $\nu = 0$ and for uniaxial stress states, the lateral stretch $\lambda_L = 1$ (see Fig. 7).

For the special case of a single fibre characterized by an uniaxial stress state, $I_{R,1}$ and J_R may be expressed by the axial (λ_R) and lateral (λ_L) stretches, using Eq. (4),

$$J_R = \lambda_R \cdot \lambda_L^2, \quad I_{R,1} = \lambda_R^2 + 2\lambda_L^2. \tag{35}$$

λ_L has to be determined from the constraint Eq. (21), which takes for this particular model the form

$$\tau_L(\lambda_R, \lambda_L) = K\ln J + G(\lambda_L^2 - \tfrac{2}{3}\ln J - 1) = 0. \tag{36}$$

Remarkably, no explicit expression for $\lambda_L = f(\lambda_R)$ can be obtained from Eq. (36).

We may, however, determine a closed form solution by rewriting Eq. (36) as

$$y + \kappa\exp(y) = \kappa - \ln\lambda_R \tag{37}$$

using the substitutions

$$y = \ln\lambda_L^2, \quad \kappa = \frac{G}{K - 2G/3} \tag{38}$$

and expanding $\exp(y)$ by a third order polynomial as

$$\exp(y) \approx \sum_{m=0}^{3} \frac{y^m}{m!}, \tag{39}$$

with $|y| < \infty$ as the interval of convergence. The closed form solution of the resulting algebraic equation of third order,

$$y^3 + 3y^2 + 6y\left(1 + \frac{1}{\kappa}\right) + \frac{6}{\kappa} \ln \lambda_R = 0 \tag{40}$$

is easily obtained from the Cardano formulae. The respective expressions for λ_L, S_R and for the uniaxial tangent modulus $E_T = 2dS_R/d\lambda_R^2$ are contained in the Appendix.

As an alternative approach, Eq. (36) may be solved by a Newton–Raphson iteration procedure. In Sect. 6 the issue of computational efficiency of both approaches will be adressed. Excellent agreement between the implicit and the explicit solution has been obtained for $0 < \lambda_R \leqq 4$.

A variant of the compressible Neo-Hookean material is characterized by a separation of volumetric and deviatoric terms in the stored energy function in the form (*Neo-Hookean Model II*)

$$W(\mathbf{C}_R) = U(J_R) + \tilde{W}(\bar{\mathbf{C}}_R) = \frac{K}{2}\left(\frac{J_R^2 - 1}{2} - \ln J_R\right) + \frac{G}{2}(\bar{I}_{R,1} - 3) \tag{41}$$

where $\bar{I}_{R,1} = J_R^{-2/3} I_{R,1}$ and $U(J_R)$ is a convex function. The constraint equation is obtained from Eq. (21) and from Eq. (41) as

$$\tau_L(\lambda_R, \lambda_L) = \frac{K}{2}(J_R^2 - 1) - \tfrac{1}{3} G J_R^{-2/3}(\lambda_R^2 - \lambda_L^2) = 0. \tag{42}$$

Again, as was noted already in the context of the model by Simo and Pister, λ_L cannot be obtained in closed form from Eq. (42). Therefore, an iterative procedure like the Newton algorithm has to be applied. We refer to Sect. 6 for a comparative computational assessment with regards to the effectiveness of the enforcement of the constraint condition Eq. (21).

The axial Second Piola Kirchoff stress and the tangent modulus are then determined from Eq. (18) and from evaluating $dS_R/d\lambda_R^2$, respectively. The respective expressions are summarized in the Appendix.

5.2 *Quadratic Logarithmic Model*

In this section, the quadratic logarithmic model is proposed as an alternative approach that completely by-passes the issue of costly iterative procedures or lengthy evaluations of algebraic expression as it is the case for the classical Neo-Hookean formulations in conjunction with uniaxial stress states. The logarithmic model has been used recently in the context of multiplicative plasticity algorithms, see e.g. Simo (1992). It is characterized by a quadratic stored energy function of the form

$$W(\mathbf{C}_R) = W(\lambda_R, \lambda_L) = \tfrac{1}{2}(K - \tfrac{2}{3}G)(\ln J_R)^2 + G[(\ln \lambda_R)^2 + 2(\ln \lambda_L)^2]. \tag{43}$$

This model fulfills the requirements for extreme strains in the sense that $W \to \infty$ as $J_R \to 0$ and $W \to \infty$ as $J_R \to \infty$. Unfortunately, however, W is *not* a convex function. Consequently, the feasibility of this formulation is restricted to the full compressive regime but, as far as tensile strains are concerned, only to moderately large strains (see Sect. 6). Despite this shortcoming, this model provides an excellent approximation for practical purposes, vastly superior to the St. Venant Model of finite elasticity. We refer to Sect. 6 for a detailed comparative evaluation.

The constraint equation

$$\tau_L(\lambda_R, \lambda_L) = (K - \tfrac{2}{3}G) \ln J_R + 2G \ln \lambda_L = 0 \tag{44}$$

yields the lateral stretch in completely analogous form to the infinitesimal theory with the strains

Table 1. Normalized CPU time consumed for the evaluation of λ_R, S_R and $dS_R/d\lambda_R^2$ using different constitutive formulations

ν	λ_R	St. Venant Model	Neo-Hooke I explicit	Neo-Hooke I iterative	Neo-Hooke II iterative	Logarithmic Model
0.0	0.5	1.0	9.0	39.7	7.1	2.7
	3.0	1.0	9.1	8.6	7.5	2.7
0.25	0.5	1.0	9.1	7.9	8.7	2.7
	3.0	1.0	8.9	7.9	8.6	2.7
0.499	0.5	1.0	8.9	5.8	9.9	2.7
	3.0	1.0	9.2	5.8	11.0	2.7

ε_R, ε_L defined now as the respective logarithmic stretches

$$\ln \lambda_L = \varepsilon_L = -\nu\varepsilon_R = -\nu \ln \lambda_R. \tag{45}$$

The axial Kirchhoff stress τ_R and the Second Piola Kirchhoff stress S_R are then obtained in the trivial form

$$\tau_R = \frac{9GK}{3K+G} \ln \lambda_R = E \ln \lambda_R, \quad S_R = E \frac{\ln \lambda_R}{\lambda_R^2}, \tag{46}$$

and the axial tangent modulus E_T is given by

$$E_T = 2\frac{dS_R}{d\lambda_R^2} = E\left[\frac{1 - \ln \lambda_R^2}{\lambda_R^4}\right]. \tag{47}$$

6 Evaluation of the models

This section contains a comparative evaluation of the different constitutive formulations investigated in Sect. 5 along with the "classical" St. Venant Model of finite elasticity, defined in the reference configuration by

$$\mathbf{S} = \left(K - \frac{2G}{3}\right) \operatorname{tr} \mathbf{E}\, \mathbf{1} + 2G\mathbf{E}, \quad \text{with} \quad \mathbf{E} = \tfrac{1}{2}(\mathbf{C} - \mathbf{1}). \tag{48}$$

We start with an assessment of the relative computational effectiveness of the models. More precisely, we compare the computer time required for the evaluation of λ_R, S_R and $dS_R/d\lambda_R^2$. This comparison includes iterative procedures altogether with the explicit expressions proposed in Sect. 5.1.

We will refer to the formulation proposed by Simo and Pister (1985) as the *Neo-Hookean Model I* and, with regards to the alternative formulation investigated in Sect. 5.1, as the *Neo-Hookean Model II*. Table 1 summarizes the relative CPU time, consumed for the evaluation of λ_R, S_R and $dS_R/d\lambda_R^2$ for different values of the poissons ratio ν and for two values of the axial stretch, $\lambda_R = 0.5$ and $\lambda_R = 3.0$, using different material models, normalized with regards to the respective CPU time required for the St. Venant Model. As far as the comparison between the iterative procedure and the explicit formulation is concerned, Table 1 reveals that, except for small values of ν, the numerical evaluation of the lengthy algebraic expressions given in the Appendix is generally more time consuming than the iterative Newton procedure. As expected, the simple expressions involved in the determination of λ_R, S_R and $dS_R/d\lambda_R^2$ for the logarithmic model make this formulation extremely attractive from the computational standpoint. The required CPU time is only $\sim 30\%$ compared to the Neo-Hookean formulations.

Figures 3–5 show the uniaxial Cauchy stress-stretch characteristics obtained for different values of Poissons ratio ν from the St. Venant Model, the Neo-Hookean Models I and II and from the logarithmic model, respectively. They illustrate the well known fact that the St. Venant Model is useless even for moderately large strains. The three hyperelastic formulations agree remarkably

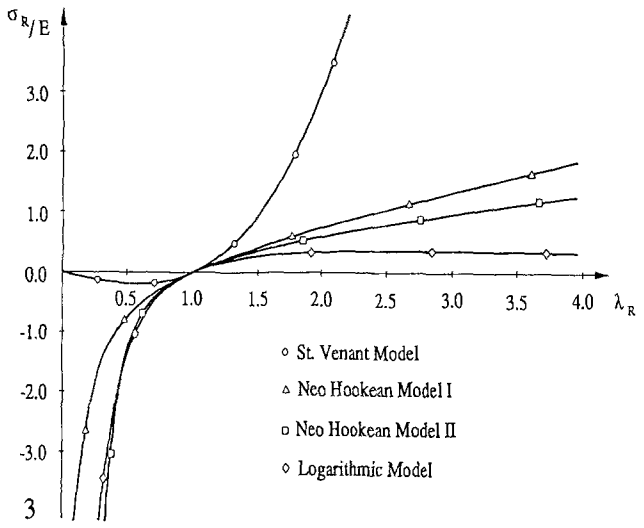

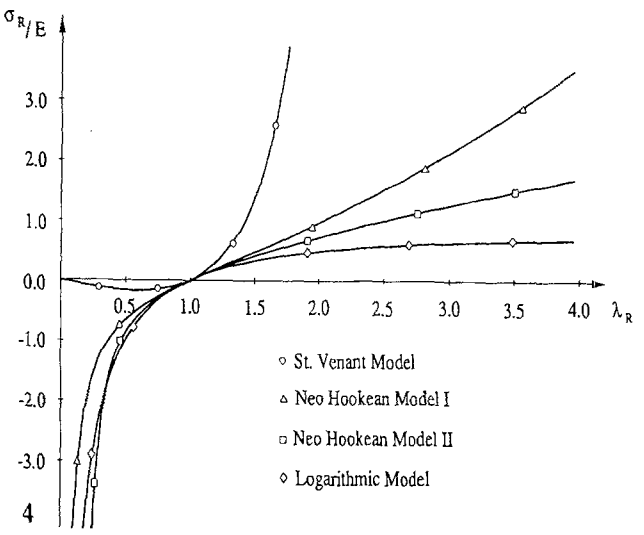

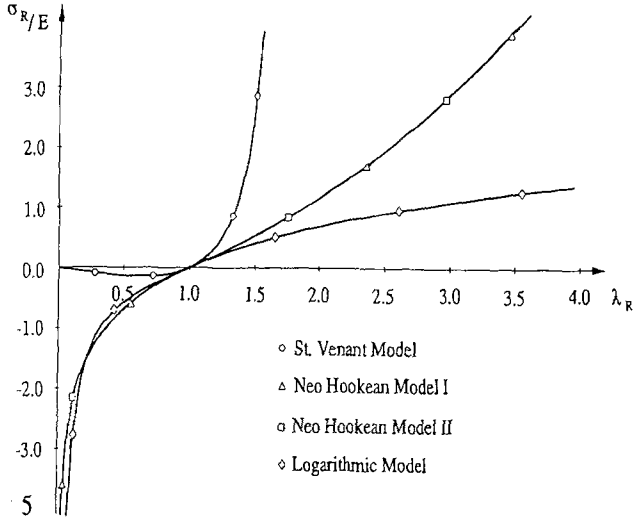

Figs. 3–5. **3** Stress-stretch characteristics for different models and $\nu = 0$. **4** Stress-stretch characteristics for different models and $\nu = 0.25$. **5** Stress-stretch characteristics for different models and $\nu = 0.5$

well in the compressive regime. When large tensile strains are involved, all three models show different $\sigma_R - \lambda_R$ characteristics. This is specially well illustrated in Fig. 4, corresponding to $\nu = 0.25$. We remark, that no attempt of an evaluation on the basis of experimental results is made in this paper, and therefore no judgement concerning the physical feasibility of the models is made here. All three models, however, show vastly superior response compared to the St. Venant Model. The logarithmic model suffers from the drawback, that for extreme strains a physically unmotivated and numerically problematic "softening" effect occurs. Fortunately, this occurs at strain levels which are irrelevant for most practical applications: softening starts at $\lambda_R = e = 2.72\ldots$ for $\nu = 0$ (Fig. 3) and at $\lambda_R = e^2 = 7.39\ldots$ for $\nu = 0.25$ (Fig. 4). No softening occurs for the incompressible case. In this case, both Neo-Hookean formulations necessarily coincide (Fig. 5), since the deviatoric part of the stored energy function coincide for $J = 1$.

Figures 6, 7, 8 and 9 contain $\lambda_R - \lambda_L$ plots for different values of ν obtained from the St. Venant Model (Fig. 6), the Neo-Hooke Model I (Fig. 7), the Neo-Hooke Model II (Fig. 8) and the logarithmic model (Fig. 9). Only the Neo-Hookean I formulation and the logarithmic model preserve the physical meaning of Poissons ratio for any value of λ_R, which implies, that $\lambda_L = 1$ for $\nu = 0$ and $(\lambda_R - 1)\cdot(\lambda_L - 1) \leqq 0$. The St. Venant Model (Fig. 6) shows the well-known pathological behaviour at large tensile strains (violation of the local inpenetrability condition) and large compressive strains (violation of the local incompressibility condition for $\nu = 0.50$). The Neo-

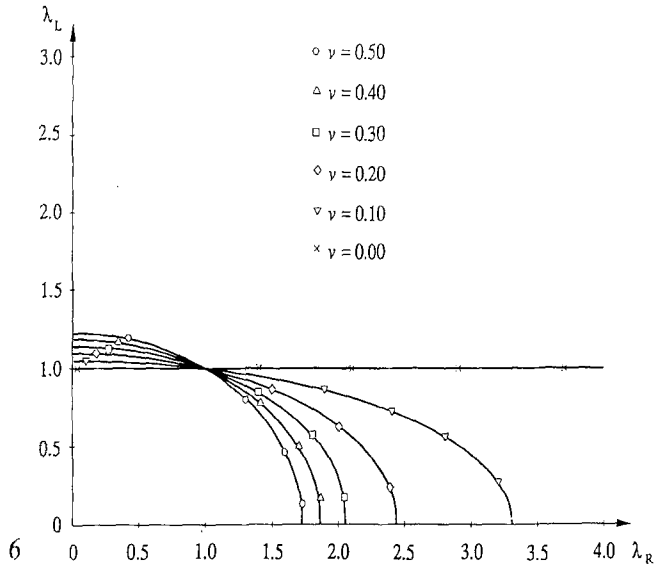

6

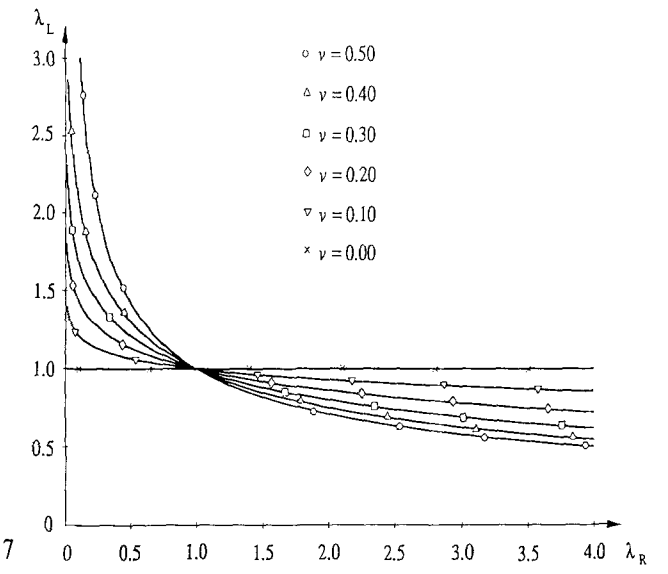

7

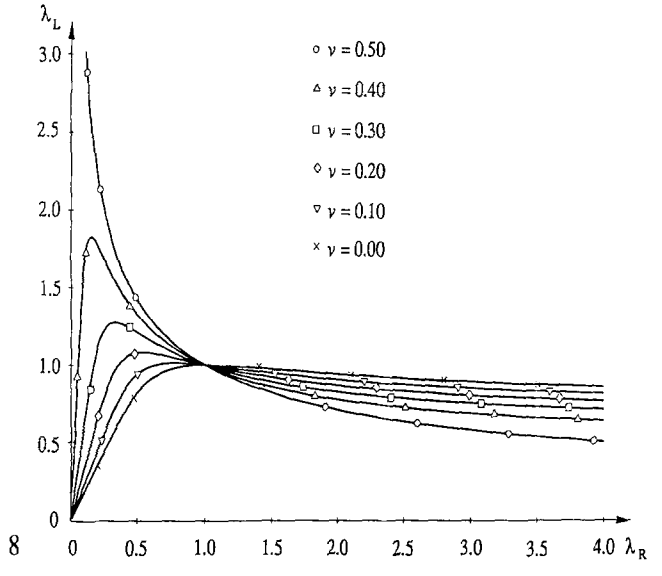

8

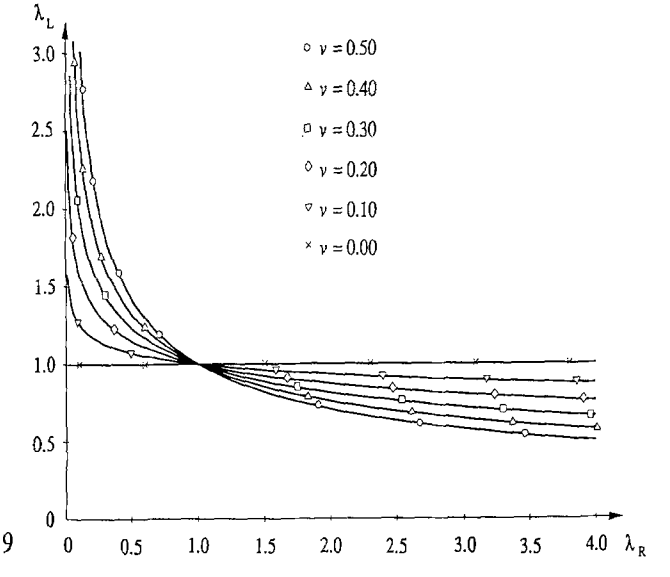

9

Figs. 6–9. **6** $\lambda_R - \lambda_L$ plots for different values of ν obtained from the St. Venant Model. **7** $\lambda_R - \lambda_L$ plots for different values of ν obtained from the Neo-Hooke Model I. **8** $\lambda_R - \lambda_L$ plots for different values of ν obtained from the Neo-Hooke Model II. **9** $\lambda_R - \lambda_L$ plots for different values of ν obtained from the Logarithmic Model

Hookean Model II, which is characterized by a complete separation of deviatoric and volumetric terms in the stored energy function, does not preserve the physical meaning of ν, since $\lambda_L \neq 1$ for $\nu = 0$. In the compressive regime, at large strains, $\lambda_L(\lambda_R)$ is not a monotonic function. The values for λ_R associated with extremal points in the $\lambda_L - \lambda_R$ curves, denoted by λ_R^*, depend on the chosen value for ν: $\lambda_R^* = 1.0$ for $\nu = 0$ and $\lambda_R^* = 0$ for $\nu = 0.5$. Hence, in the incompressible limit, this defect vanishes. Due to this pathological behavior, attention has to be paid with respect to the choice of the elasticity moduli when using the Neo-Hookean II formulation.

In the incompressible limit, all models except the St. Venant model yield identical $\lambda_R - \lambda_L$ plots, since the constraint conditions Eqs. 36, 42 and 44 induce that $J \to 1$ as $G/K \to 0$.

7 Numerical simulations

This chapter contains an application of the different material models to 3D-finite element analysis of a sandwich rubber plate. The plate is reinforced by two pairs of diagonally oriented cord layers,

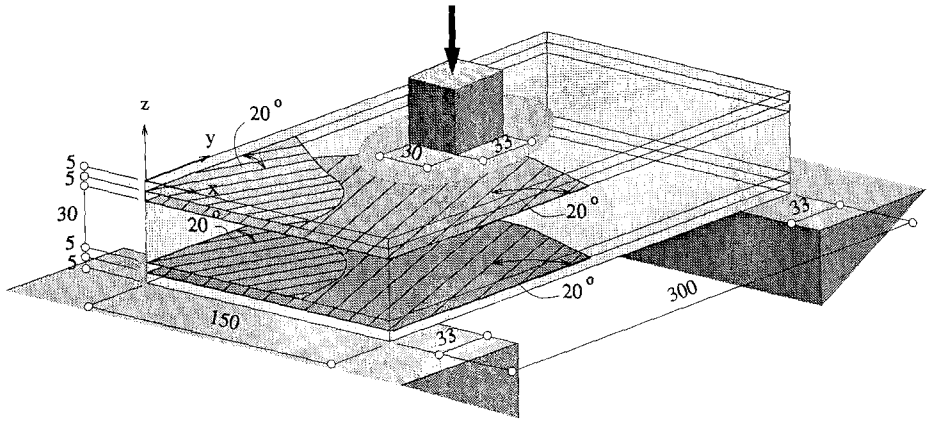

Fig. 10. Sandwich slab subjected to punch indentation (dimensions: mm)

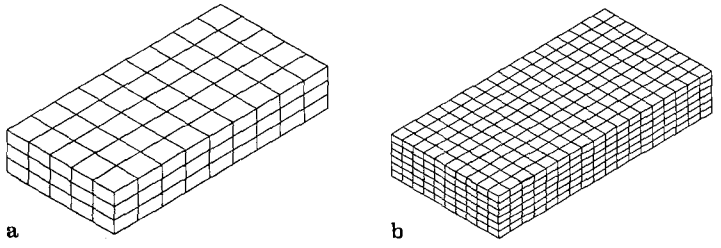

Fig. 11a, b. Finite element model of the sandwich slab: **a** coarse mesh, **b** fine mesh

each pair located parallel to the top and the bottom surface of the slab (Fig. 10). The angle between the y-axis and the cords is $\pm 20°$. The rubber plate is subjected to an indentation of a rectangular rigid punch located at the center of the slab (Fig. 10).

The goal of this simulation is a comparative evaluation with respect to the structural behaviour predicted by the different material formulations discussed in chapter 5. The rubber matrix material is modelled by the Mooney Material Law with the Mooney-parameters taken as $C_1 = 1.0\,\mathrm{kN/cm^2}$, $C_2 = 0.333\,\mathrm{kN/cm^2}$. The material parameters for the cords are taken as $E_R = 1000.0\,\mathrm{kN/cm^2}$, $\nu = 0.25$. As far as the rubber matrix material is concerned, the condition of incompressibility is enforced by the lagrange multiplier method. The geometric boundary conditions are defined by fixed displacements in y and z-direction at all points at the lower surface within a distance of 33 cm from both edges of the plate, thus simulating the plate as being "glued" to a rigid surface. Fig. 10 contains the geometry of the sandwich plate, the location of the rigid punch, and the boundary conditions.

Three finite element models characterized by different degree of discretization are used in the calculations: Meshes A and C are based on 8-node elements for the cords and for the matrix material, respectively. Mesh B uses 20 node elements. The coarse meshes A and B (Fig. 11a) contain 135 incompressible and 90 rebar elements, the consistently refined mesh C (Fig. 11b) contains 1080 incompressible elements and 720 rebar elements. In the coarse mesh, the rebar elements are located at the top and the bottom of the plate, representing 2 layers of reinforcement each. In the fine mesh, each cord layer is modelled separately by one layer of rebar elements near both surfaces.

Figures 12 and 13 show the deformed shape of the sandwich slab at $u = 6\,\mathrm{cm}$ obtained from mesh A (Fig. 12) and from mesh C (Fig. 13). Figures 12a and 13a clearly show the distortion of the plate induced by the reinforcing plies.

Figure 14 contains the load–displacement curves obtained from numerical analyses of the slab using different meshes and different material models for the cords, namely the St. Venant Model, two Neo-Hookean formulations and the logarithmic model. For comparison, a u-P-curve obtained from an analysis of the rubber plate without cord-reinforcement is included in Fig. 14. As far as the influence of the particular material model with respect to the structural behaviour of the sandwich plate is concerned, the St. Venant Model shows a slightly stiffer response

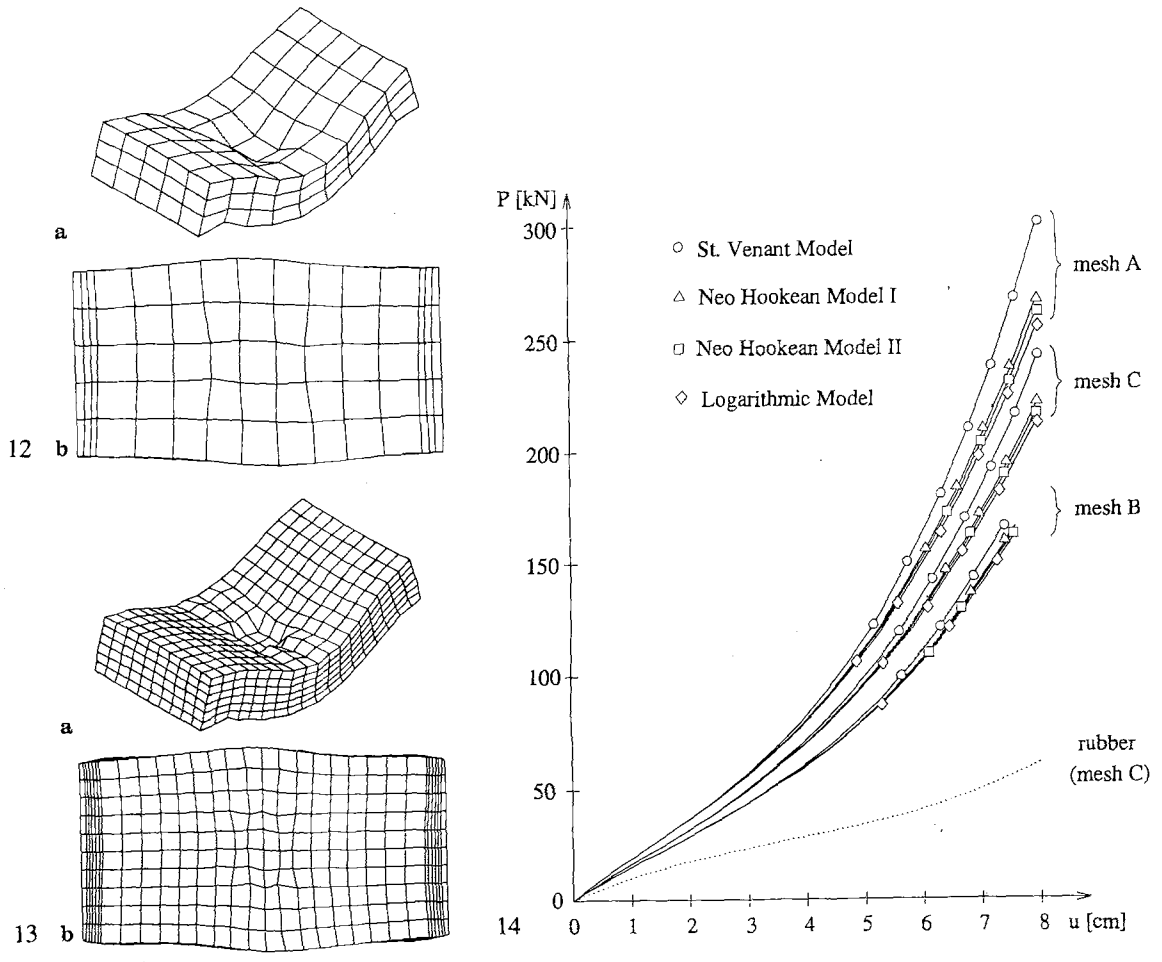

Figs. 12–14. **12a, b** Deformed plots of the sandwich slab obtained from mesh A at $u = 6$ cm. **13a, b** Deformed plots of the sandwich slab obtained from mesh C at $u = 6$ cm. **14** Load-displacement curves obtained from different material models for the reinforcing fibres

relative to the Neo-Hookean models and to the logarithmic model, respectively. The relative difference between these three models is negligeable.

This result indicates that the more sophisticated models, like the Neo-Hookean formulations, do not improve the physical representation of reinforcing cords in FE simulations when compared to the quadratic logarithmic model. Taking into consideration the numerical inefficiency of the Neo-Hookean Models when degenerated to uniaxial stress states, the logarithmic model seems to be the adequate choice for the representation of reinforcing cords in the framework of rebar elements.

8 Conclusions

The paper revisits the technique of representing reinforcing cords in composite materials by means of overlay ("rebar") elements in the context of large strain finite element analyses. The cord layers are represented by bundles of parallel fibres characterized by uniaxial stress states, with the in-plane shear stiffness being neglected.

The kinematics and variational formulation of rebar elements is presented in the frame-work of finite strain hyperelasticity. Three hyperelastic material formulations are discussed. It turns out, that the special case of uniaxial stress states is not obtained in a trivial form from the general threedimensional format of the compressible Neo-Hookean formulations. For a particular form of this class of material laws explicit expressions for the axial stress-stretch relationship altogether

with the uniaxial tangent modulus are given. An alternative formulation that completely by-passes this cumbersome issue is proposed by means of the quadratic logarithmic model. Due to its simplicity, this model is computionally very efficient and suitable for applications involving large, although not extremely large, strains.

A comparative evaluation of three hyperelastic constitutive models along with the "classical" St. Venant Model is concerned with the computational effectiveness, the physical plausibility and the uniaxial stress-stretch characteristics of the different models at large strains.

The performance of rebar elements in conjunction with hyperelastic formulations is illustrated by means of a numerical simulation of a cord-reinforced sandwich rubber slab. This simulation reveals, that the most simple model available for finite elasticity theories—the logarithmic model—is ideally suited for the bulk of practical applications involving cord-reinforced composite materials.

Appendix

This Appendix contains a summary of the expressions for the function of stored energy, W, the axial Second Piola-Kirchhoff stress, S_R, and the uniaxial material tangent modulus E_T for the St. Venant Model, the Neo-Hookean Model I according to Simo and Pister (1985), the Neo-Hookean Model II and for the logarithmic model, respectively.

St. Venant Model

$$W = \tfrac{1}{2}(K - \tfrac{2}{3}G)(\operatorname{tr}\mathbf{E})^2 + G\mathbf{E}:\mathbf{E},$$

$$S_R = \tfrac{1}{2}E_T(\lambda_R^2 - 1),$$

$$E_T = \frac{9KG}{3K+G} = \text{const.}$$

Neo-Hookean Model I

$$W = \tfrac{1}{2}(K - \tfrac{2}{3}G)(\ln J_R)^2 - G\ln J_R + \tfrac{1}{2}G(I_{R,1} - 3),$$

$$S_R = [(K - \tfrac{2}{3}G)\ln J_R + G(\lambda_R^2 - 1)]/\lambda_R^2,$$

$$E_T = \left[(K - \tfrac{2}{3}G)(1 - 2\ln J_R) + 2G - \frac{(K - \tfrac{2}{3}G)^2}{(K - \tfrac{2}{3}G) + G\lambda_L^2}\right] \Big/ \lambda_R^3,$$

$\lambda_L = f(\lambda_R)$ is determined from (36).

With respect to the explicit formulation proposed in Sect. 5, expressions for λ_L, S_R and E_t are obtained as

$$\alpha = 2G/3K, \quad \beta = 6\sqrt{3\alpha}[1 - (1-\alpha)\ln\lambda_R],$$

$$\gamma = \frac{\beta}{\sqrt{\beta^2 + (4-\alpha)^3}}, \quad \delta = \left(\frac{1+\gamma}{1-\gamma}\right)^{1/6},$$

$$\zeta = \sqrt{\frac{4-\alpha}{3\alpha}}(\delta - 1/\delta), \quad J = \lambda_R \exp(\zeta),$$

$$S_R = K(1-\alpha)\frac{\ln J}{\lambda_R^2} + G(1 - 1/\lambda_R^2), \quad \lambda_L = \exp(\zeta/2),$$

$$E_T = \frac{K(1-\alpha)}{\lambda_R^4}\left(1 - 2\ln J - 2(\delta + 1/\delta)\frac{(1-\alpha)\sqrt{4-\alpha}}{\beta^2 + (4-\alpha)^3}\right) + \frac{\beta G}{\lambda_R^4}.$$

Neo-Hookean Model II

$$W = \tfrac{1}{2}K\left(\frac{J_R^2 - 1}{2} - \ln J_R\right) + \frac{G}{2}(\bar{I}_{R,1} - 3),$$

$$S_R = \frac{3K}{2\lambda_R^2}(J_R^2 - 1)$$

$$E_T = \frac{K}{\lambda_R^4}\left[\frac{6J_R^2(1 - J_R^2) + \kappa(2\bar{\lambda}_R^2 - \bar{\lambda}_L^2)(2J_R^2 + 1)}{2J_R^2 + \frac{\kappa}{3}(2\bar{\lambda}_R^2 - \bar{\lambda}_L^2)}\right],$$

where $\kappa = \dfrac{2G}{3K}$, $\bar{\lambda}_R = J^{-1/3}\lambda_R$, $\bar{\lambda}_L = J^{-1/3}\lambda_L$ and $\lambda_L = f(\lambda_R)$ is determined from (42).

Logarithmic Model

$$W = \tfrac{1}{2}(K - \tfrac{2}{3}G)(\ln J_R)^2 + G[(\ln \lambda_R)^2 + 2(\ln \lambda_L)^2],$$

$$S_R = \frac{9KG}{3K + G}\frac{\ln \lambda_R}{\lambda_R^2},$$

$$E_T = \frac{9KG}{3K + G}\left[\frac{(1 - \ln \lambda_R^2)}{\lambda_R^4}\right], \quad \text{with}$$

$$\ln \lambda_L = -\nu \ln \lambda_R.$$

References

Ciarlet, P. G. (1981): Three-dimensional mathematical elasticity. North-Holland, Amsterdam

Helnwein, P.; Liu, C. H.; Meschke, G.; Mang, H. A. (1993): A new 3D-FE-model of cord-reinforced composites. Application to analysis of automobile tires. Finite Elements in Analysis and Design, 14 (1993), 1–16

Mang, H. A.; Meschke, G. (1991): Finite element analyses of reinforced and prestressed concrete structures. Engineering Structures 13, 211–226

Noor, A. K.; Tanner, J. A. (1985): Advances and trends in the development of computational models for tires. Computers and Structures 20, 517–533

Reddy, J. N. (1989): On refined computational models of composite laminates. Int. J. Num. Meth. Eng. 27, 361–382

Tabaddor, F.; Stafford, J. R. (1985): Some aspects of rubber finite element analysis. Computers and Structures 21, 327–339

Simo, J. C.; Pister, K. S. (1985): Remarks on rate constitutive equations for finite deformation problems. Comput. Meth. Appl. Mech. Eng. 48, 201–215

Simo, J. C. (1992): Algorithms for static and dynamic multiplicative plasticity that preserve the classical return mapping schemes of the infinitesimal theory. Comp. Meth. Appl. Mech. Eng. 99, 61–112

Walter, J. D. (1978): Cord-rubber tire composites: theory and applications. Rubb. Chem. Technol. 51, 524–576

Communicated by H. A. Mang, June 28, 1993